Nanoscale

PAPER

View Article Online
View Journal | View Issue

Cite this: *Nanoscale*, 2025, **17**, 21737

Room-temperature negative differential resistance in single-atom devices

Vladislav V. Shorokhov, [a,b] Denis E. Presnov, [a,b] Ilia D. Kopchinskii, [b] Andrey A. Shemukhin, [b,c] Natalia S. Maslova, [b] Vladimir N. Mantsevich, [a,b] Artem S. Trifonov, [a,b] Yuri A. Pashkin, *[d] Oleg V. Snigirev[a,b] and Vladimir A. Krupenin *[a,b]

We report the observation of negative differential resistance (NDR) in single-atom single-electron devices based on arsenic, phosphorus and potassium dopants implanted in a silicon host matrix. All devices exhibit NDR, with the potassium-based one exhibiting NDR at room temperature because of the larger charging and confinement energies. Our experimental results are reproduced with a simple model that assumes sequential electron tunnelling through two series-connected charge centres, each having two discrete energy levels. The model utilises the nonequilibrium Keldysh diagram technique, and its accuracy is improved by introducing an effective local temperature that depends on the dissipated power and by semi-classical averaging of fluctuations of the dopant spectra. Our control experiments on undoped devices revealed the bandgap boundaries of the silicon host matrix which we successfully modelled using a single-barrier approximation. The use of unconventional dopants in silicon with high characteristic energies, such as potassium, is a major step forward toward the implementation of room-temperature single-atom electronics.

Received 13th March 2025,
Accepted 29th August 2025

DOI: 10.1039/d5nr01075f

rsc.li/nanoscale

Introduction

Negative differential resistance (NDR) is the property of some nonlinear electronic components, in which an increase in voltage across its terminals results in a decrease in electric current through it, producing a negative slope on the current–voltage characteristic.[1] NDR plays a key role in building many electronic devices such as AC generators and amplifiers, switchers, memory circuits, *etc.*[2] In semiconductor structures, the mechanism of NDR is related to the tunnelling of charges through multiple potential barriers when the tunnelling probability depends on the applied voltages. The essential ingredients of NDR are well-defined energy levels created by doping in heterostructures[3] or spatial quantisation in quantum dots.[4]

Recently, due to the progress in nanofabrication, it became possible to create electronic devices whose operation is based on single molecules[5] and atoms.[6] In such structures, the energy levels are inherently discrete because of quantum confinement and strong Coulomb effects, which makes them promising for the observation of NDR. However, the temperature range in which NDR can be observed depends on the characteristic energy scale of particular structures. Experiments on single-molecule devices report NDR observations in a wide temperature range.[7–15] A typical NDR mechanism in such devices is charge tunnelling between two energy levels corresponding to different spatial localisations of electron densities, which are in resonance at a certain value of the applied bias and out of resonance at other values.

An alternative explanation of NDR in molecular structures was proposed in ref. 16. The authors attributed the formation of NDR to the enhancement of one of the two tunnel barriers of the molecular single-electron transistor by the source–drain electric field. This interpretation was used to explain the experimental results reported previously.[10,12] However, the proposed mechanism cannot explain the formation of NDR in strongly correlated small-size systems[17] where the strong Coulomb interaction plays an important role and should be taken into account. It was shown later that strongly correlated low-dimensional structures, including single-electron devices, exhibit NDR due to the presence of both strong Coulomb interactions and asymmetry between relaxation rates in tunnel junctions.[18–20]

The ultimate electronic device is one in which gate-controlled electron transport occurs through a single atom

[a]*Quantum Technology Centre, Faculty of Physics, Lomonosov Moscow State University, Leninskie Gory, 1(2), Moscow, 119991, Russia.*
E-mail: krupenin@physics.msu.ru
[b]*Lomonosov Moscow State University, Faculty of Physics, Leninskie Gory, 1(2), Moscow, 119991, Russia*
[c]*D.V. Skobeltsyn Institute of Nuclear Physics, Lomonosov Moscow State University, Leninskie Gory, 1(2), Moscow, 119991, Russia*
[d]*Department of Physics, Lancaster University, Lancaster LA1 4YB, UK.*
E-mail: y.pashkin@lancaster.ac.uk

coupled to the source and drain electrodes. The first single-atom single-electron transistor was built by placing a transition metal complex in the gap between the two electrodes, with a gate electrode located under the entire structure.[21] A more technologically viable approach is to use doping, *i.e.*, the intentional introduction of impurities into an intrinsic semiconductor, which is commonly used for the purpose of modulating its electrical, optical and structural properties. The doping process introduces allowed states within the band gap whose position depends on the host semiconductor and the dopant used, and determines the binding energy, which, for conventional dopants like arsenic and phosphorus, is much smaller than the energy gap of the host semiconductor.

Arsenic and phosphorus are widely used in the semiconductor industry as donor dopants in silicon, therefore their properties have been studied extensively.[2] Their electric and electron transport properties as well as the valence electron binding energy are well understood and were discussed previously[22,23] (see also references therein). The binding energy of a phosphorus dopant in silicon is $\varepsilon_P \simeq 46$ meV and the size of the corresponding charge centre is $r_P \simeq 2.5$ nm that gives the charging energy $E_C^P = e^2/2C \simeq 25$ meV. The corresponding parameters for an arsenic dopant in silicon are $\varepsilon_{As} \simeq 54$ meV, $r_{As} \simeq 3.9$ nm and $E_C^{As} \simeq 16$ meV.

In contrast, potassium ions are rarely used for implantation in silicon and silicon dioxide (see SI). This dopant is of particular interest for building single-atom devices because its electron and hole energy levels in a Si matrix are located in the middle of the band gap. In addition, this dopant has a small effective size of the charge centre and, as a result, high charging energy. Hence, the operation temperature of K-based devices is expected to be much higher than that of their P and As analogues.

Potassium behaves as a donor when implanted in silicon; however, donor levels and electrical properties strongly depend on the dopant location in the Si crystal lattice. Data on the binding energy of potassium dopants in silicon is scarce and varies greatly: from $\varepsilon_K = 0.04$ eV (ref. 24 and 25) up to $\varepsilon_K = 0.26$ eV.[3,p. 23] Such a large variation of the binding energy could be due to the different methods of sample preparation and ion implantation. From these values, one can estimate that the charging energy of a K dopant in silicon is as high as 330 meV, which warrants room-temperature device operation (see SI).

Although single-atom single-electron devices based on single As and P dopants have been demonstrated by several groups,[22,23,26–32] so far there have been no reports on devices in which electron transport occurs through charge states of a single K atom. Here we present three types of single-atom devices in which phosphorus, arsenic and potassium atoms are used as dopants. All three demonstrate NDR, and the device doped with potassium shows NDR even at room temperature due to a much larger charging energy of K as compared to conventional dopants. We model charge transport through the devices assuming sequential electron tunnelling through two series-connected charge centres, each having two discrete energy levels. The excellent agreement of the measured data and simulation results for all devices confirms sequential electron tunnelling through individual dopant centres as the origin of the observed NDR.

Results and discussion

The samples measured in this work were fabricated using the nanofabrication techniques detailed in the Methods section. The key element of all devices is a narrow constriction, called a nanobridge, etched in the layer of silicon on silicon oxide, as shown in Fig. 1. The nanobridge contains dopant atoms of P, As or K. For detailed characterisation, chips with single-atom devices were placed in a shielded chip holder and bonded using Al wires. The devices were characterised at 4.2 K (those based on P and As) or at room temperature (device based on K) by measuring the DC current (I) as a function of the bias voltage (V) and gate voltage (V_G).

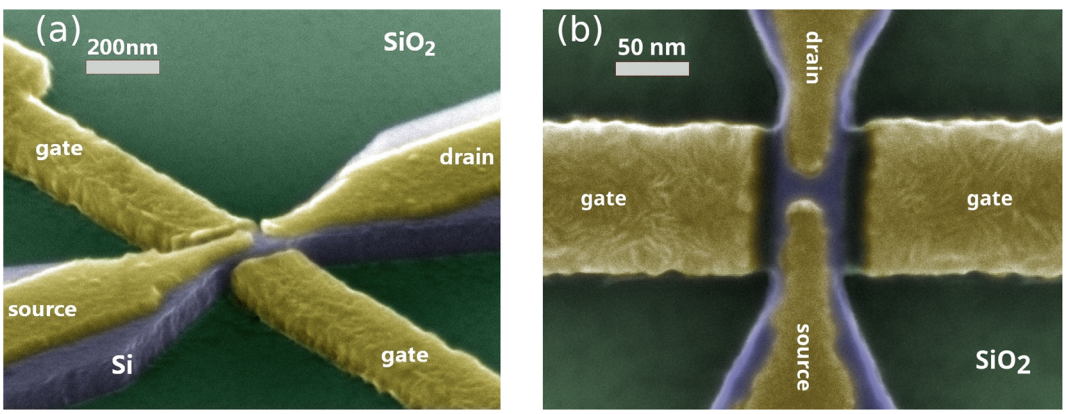

Fig. 1 False colour images of single-atom single-electron device structure in a scanning electron microscope. (a) Side view. (b) Top view. Blue colour denotes the silicon layer; green—the insulating layer of silicon dioxide; dark-yellow—the chromium source, drain and gate electrodes. The estimated gap between the source and drain is ~20 nm and the gap between the gate electrodes and nanobridge is ~10 nm. Note the sloped inner faces of the gate electrodes in (b): the bottom edge of each gate is closer to the nanobridge than its top edge.

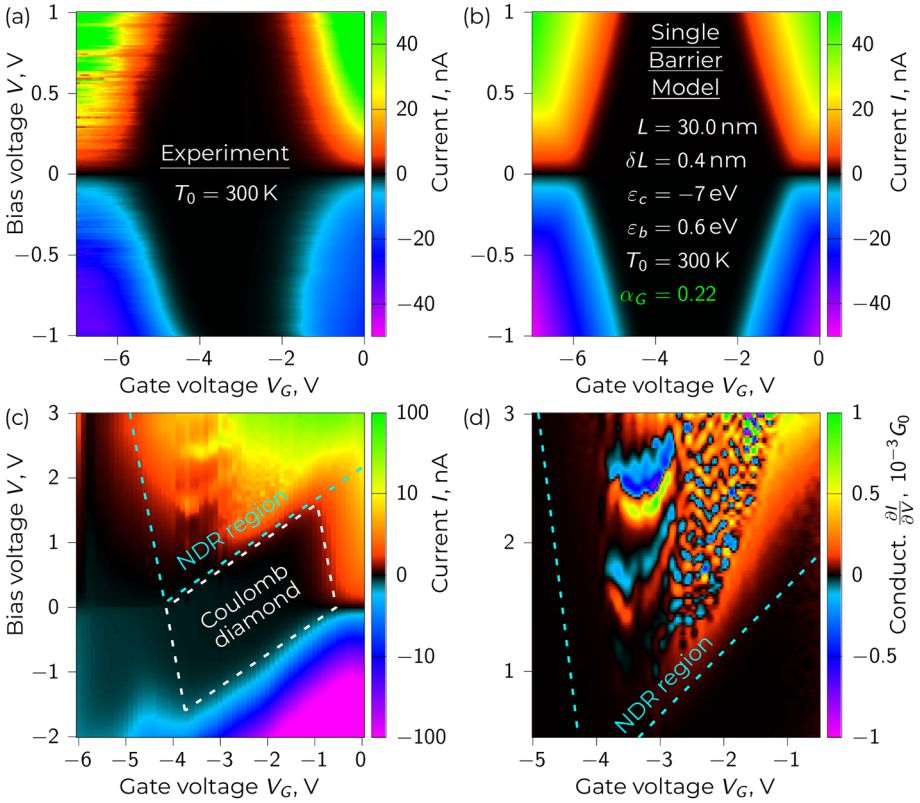

Fig. 2 (a) Electric current through the undoped silicon nanobridge as a function of bias voltage V and gate voltage V_G. (b) Electric current calculated using the single-barrier model (see also Fig. 3a). The model fitting parameters are: L = 30 nm, δL = 0.4 nm, ε_c = −7 eV, ε_b = −0.6 eV, A_0 = 1.3 × 10^{-3} and electrostatic gate lever α_G = 0.22. (c) Electric current and (d) differential conductance $\partial I/\partial V$ of the K-doped silicon nanobridge as a function of bias voltage V and gate voltage V_G at room temperature. The dashed lines indicate the regions of Coulomb blockade (white) and NDR (cyan).

We start with a comparison of charge transport through two nanobridges of nominally the same dimensions: one is an intrinsic Si device and the other is a device built of Si doped with K, see Fig. 2. Because differential conductance and differential resistance are interrelated, we will use both quantities when discussing our experimental data.

Fig. 2a shows the measured tunnelling current, $I(V, V_G)$, through the undoped silicon nanobridge as a function of the bias and gate voltages. The growth of the current on the right and on the left is caused by the induced electron and hole conductivity. It is really remarkable that regions with two different types of conductivity were measured in the same experiment, which was possible due to the small length of the nanobridge (<100 nm) and the close proximity of the gate electrodes. In addition, one can see that the diagram is almost symmetric with respect to the horizontal axis V = 0, which indicates that the intrinsic silicon nanobridge is homogeneous and therefore the effect of the gate potential is the same for positive and negative source–drain voltages. At these values of V and V_G, the current through Si is small, without having any distinct periodic features, and provides just a background for the single-electron current. Using the slope of the line corresponding to the onset of current on the right, we estimate the gate to source–drain leverage for electrons being $\Delta V/\Delta V_G \approx 1.3$. By performing the same procedure for the region on the left, we estimate the gate to source–drain leverage for holes to be $\Delta V/\Delta V_G \approx 0.2$. The different values of the lever arm for electrons and holes can be explained by the different mobilities of the charge carriers. We associate the region at zero bias and between −5 V up to about −2 V of the gate voltage as the region without conductance which corresponds to the silicon energy band gap. Importantly, K deep dopant levels are located in the band gap[2] and we observe single-electron effects in this region when the nanobridge is doped with K atoms.

The conduction of the undoped nanobridge can be described with the help of a simple single-barrier model with a smoothed barrier, as shown in Fig. 3a. For simplicity, we assume that tunnelling current through the barrier is proportional to the integral of the transmission coefficient over the Fermi window, *i.e.* we use a variant of the Meir–Wingreen formula:[33]

$$I(V, V_G) = A_0 \frac{e}{\pi\hbar} \int \tau(\varepsilon, V, V_G)[f_L(\varepsilon, V) - f_R(\varepsilon, V)]\mathrm{d}\varepsilon, \qquad (1)$$

with the standard Fermi distributions $f_{L(R)}(\varepsilon, V) = \left[1 + \exp\left(\frac{\varepsilon \mp eV/2}{k_B T_0}\right)\right]^{-1}$ in the left and right electrodes and a dimensionless scaling factor A_0 depending on the effective densities of states (DOS) in the electrodes and the geometry of

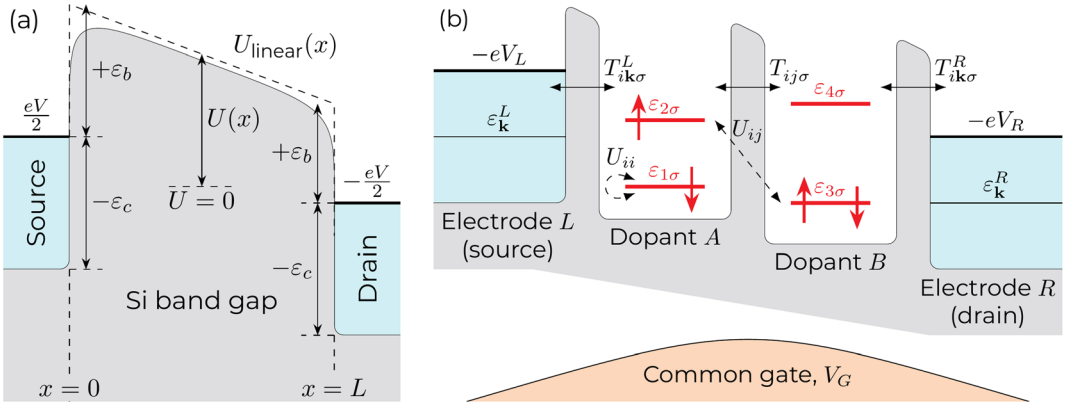

Fig. 3 (a) Schematic energy diagram for the single-barrier model. The parameters used in the model are evident from the sketch (see also Fig. 2b). (b) Energy diagram of the two-dopant model comprising two localised states with two energy levels in each state, nicknamed as "2D × 2L" (see subsection Theoretical model for detailed description and notations).

the nanobridge. The barrier transmission coefficient $\tau(\varepsilon, V, V_G)$ has contributions from both electrons and holes and is calculated numerically as the quantum-mechanical transparency of the smoothed barrier. This calculation involves a numerical solution of the one-dimensional Schrödinger equation with a potential energy $U(x)$ of the smoothed barrier. Barrier smoothing originates from image force correction: a tunnelling charge experiences attraction to its mirror image on the electrodes, effectively lowering the barrier height in the vicinity of the source and drain, $U(x) = U_{\text{linear}}(x) + \delta U(x)$. In order to prevent the Coulomb attraction potential $\delta U(x)$ from diverging at the interfaces, $x = 0$ and $x = L$, we introduce a small coordinate correction δL so that $\delta U(x) \propto -1/(x + \delta L) - 1/(L - x + \delta L)$. This correction was found to be 0.4 nm which is much smaller than the barrier length $L = 30$ nm. Physically, δL can be attributed to the uncertainty of the barrier length in the fabricated device and to the model assumption that the tunnelling charges are described with the distributed wave functions. The charge images in the electrodes are not the point charges either, hence they must be treated in a similar way.

This simple model reproduces reasonably well the experimental current diagram presented in Fig. 2b. The fitting of the current diagram allowed us to estimate the electrostatic lever of the gate electrode to be about $\alpha_G = 0.22$ under the assumption that the undoped nanobridge silicon is characterised by its bulk band gap value $E_g = 1.17$ eV. Therefore, in our experimental setup, a change of gate voltage ΔV_G gives rise to a five-time weaker change $\alpha_G \Delta V_G$ of the nanobridge energy structure. We believe that some roundness of the edges of the non-zero current region in Fig. 2a is not perfectly reproduced within the model current diagram in Fig. 2b due to the neglected Coulomb interaction between the distributed tunnelling electrons and because of the simplified current formula (1) which does not account for the quasiparticle DOS in the electrodes.

The behaviour of the electric current and the differential conductance becomes drastically different for the Si nanobridge doped with K, see Fig. 2c and d, respectively. The current stability diagram presented in Fig. 2c reflects a multitude of distinct processes occurring within the nanobridge. As we propose, there is a region on the V–V_G plane in which only one dopant is involved in charge transport, but the tunnel current is completely blocked, forming a characteristic Coulomb diamond. The size of the Coulomb diamond gives us an estimate of the characteristic voltage V_C of the Coulomb blockade which is half the size of the Coulomb diamond along the V axis. Clearly, this value is about $V_C \simeq 1.6$ V, which is due to a single-electron transport *via* an individual potassium dopant. The corresponding charging energy together with confinement energy $(\Delta\tilde{\varepsilon})\, E_C + \Delta\tilde{\varepsilon} = eV_C/2 = 0.8$ eV is of the same order as our *a priori* estimate $E_C \sim 330$ meV (see SI). It is very unlikely that positively charged K dopants could form a small island with a comparable charging energy given Coulomb repulsion between the dopants. Just outside the Coulomb diamond at more positive bias voltage, energy levels of a neighbour dopant become activated in the nanobridge and charge transport takes place through two dopants connected in series. When the energy levels line up the tunnelling rate increases giving a lower tunnel resistance. At even higher bias voltage the levels detune which results in a higher tunnel resistance. Such alignment and misalignment of energy levels between the neighbouring dopants repeat as the bias voltage increases further. This manifests as the emergence of the negative differential resistance microstructure in a certain range of the bias and gate voltages just outside the Coulomb diamond. We note that because of the many factors involved in charge transport, such as the different energy level structure in the neighbouring dopants, one cannot expect NDR to manifest symmetrically at positive and negative bias.

The differential conductance varies by many orders of magnitude and even becomes negative. The black area in Fig. 2d corresponds to the vanishingly small conductance, $10^{-6}G_0$ ($G_0 = 2e^2/\hbar$ being the conductance quantum) and lower. The conductance grows rapidly on the right side of Fig. 2d, therefore V_G is limited to −1 V in it. There is a gentler increase in conductance at $V_G < -5$ V. One can see that the characteristic region with non-zero conductance (enclosed by a cyan dashed

line in Fig. 2c and d) is very close to a triangular shape, which is specific to single-electron tunnelling. At the same time, this triangle-like region contains well-pronounced features with a strongly varying differential conductance. The positive conductance alternates with the negative conductance, which corresponds to peaks and dips in the current–voltage characteristic. We attribute this behaviour to the presence of at least two discrete energy levels between the source and drain electrodes (extending the model,[34] see details below). These features appear to be periodic in the bias voltage, however, the period is very different on the left and on the right, with the crossover from one to the other taking place at about −3 V. Although this sharp transition from one regime to the other is not fully understood, we believe that the small-amplitude oscillations can be associated with the involvement of higher density energy levels in charge transport when the gate voltage is changed. This effect can be enhanced by band bending, which can be tuned by both the gate and bias voltages.

The observed negative differential resistance can be explained by considering a conduction channel with at least two localised states connected in series between the source and drain electrodes capacitively coupled to the common side gate electrode (see the spatial energy diagram in Fig. 3b). The two localised states may correspond to individual impurity atoms situated close to each other in the semiconductor matrix. Since As, P and K atoms serve as donors, each dopant is electrically neutral only when its valence electrons are captured. Under finite temperature and bias voltage, dopants donate their valence electrons freeing some of the localisation sites. Electronic transport proceeds as follows: a delocalised electronic quasiparticle near the surface of the source electrode's tip transforms into an electron that tunnels to the nearest positively charged dopant. Electron tunnelling also enables hopping between localisation sites. Finally, an electron localised in the other dopant tunnels into the drain electrode and excites a new quasiparticle there.

Apart from quantum-mechanical tunnelling, one has to take into account the Coulomb interaction. Depending on the effective localisation length Δl (which differs by orders of magnitude for the near-surface and deeply buried dopant atoms), Coulomb repulsion between the localised electrons may have different strengths scaling as $1/\Delta l$. As long as the dopants are randomly scattered at various depths in the SiO_x/Si interface, we treat all length scales (including localisation lengths) as free fitting parameters of our model. Even the distance between the source and drain electrodes is not known exactly *a priori* because the electrode tips, as seen in the SEM image of Fig. 1, can be extended with tightly clustered dopants concentrating near the electrode surface. In a nanoscale structure, material properties such as permittivity ε may also deviate significantly from their handbook bulk values and must be treated as fitting parameters. Furthermore, the energy levels spacing $\Delta\tilde{\varepsilon}$ of the dopants due to quantum confinement strongly depends on the unknown localisation length and the way each dopant atom is incorporated into the semiconductor matrix, thus $\Delta\tilde{\varepsilon}$ becomes a subject of optimisation as well.

Since the measured *I–V* curves exhibit two current peaks, we include two spin-degenerate discrete energy levels in the spectrum of each dopant. The resulting energy spectrum of the 2D × 2L system as a whole is affected by Coulomb interaction and the formation of hybridised quantum states due to quantum-mechanical tunnelling between dopants. We use the non-equilibrium diagram technique[35,36] to model the electron transport between the two electrodes-reservoirs through the open quantum system of two sequential double-level localised states; see subsection Theoretical model for details. For the given bias and gate voltages and using the set of fitting parameters, we calculate the tunnel current in the stationary regime. Separately, we find and subtract the background current I_{bg} as a function of V described by the exponential function $I_{bg}(V) = I_{00} + I_0\left[\exp\left(\frac{V}{V_0}\right) - 1\right]$, where I_{00} is the offset current, I_0 and V_0 are the fitting parameters that represent typical scales of the background *I–V* curve. Then we adjust the fitting parameters of dopants to obtain the best agreement between the measured and modelled *I–V* characteristics for three devices based on As, K and P.

The results of fitting are presented in Fig. 4 and 5, with the best-fit parameters listed in Table 1. The model provides a reasonable approximation for the measured data and explains the observed current peaks as follows. The electric field between the source and drain electrodes changes the energy spectra of both dopants differently, and once a pair of energy levels aligns as shown in Fig. 4b, hybridisation of the corresponding quantum states becomes almost symmetric—that is, the tunnelling rates between the resulting hybridised states and each of the electrodes (kinetic coefficients) grow comparable to each other. Consequently, a wider conduction channel opens which we observe in the form of the resonance-like current peak. Further growth of the bias voltage increases the offset between the single-particle energy levels and brings them off the resonance. The increased energy misalignment breaks the symmetry of hybridisation and couples the hybridised states to the source and drain electrodes unequally, so the smallest of the tunnelling rates becomes a bottleneck for the electron transport. This disruption of resonance closes the conduction channel and makes a negative contribution to the overall differential conductance. Evidently, this resonant mechanism of NDR is influenced by the Coulomb interaction, which modifies the spectra of the dopants while shifting the original single-particle energy levels $\tilde{\varepsilon}_{i\sigma}$ to their renormalised values $\tilde{\varepsilon}_{i\sigma} \sim \varepsilon_{i\sigma} + \sum_j U_{ij}$ (see subsection Coulomb energies of the SI for details). In the case of shorter localisation lengths (stronger Coulomb interaction), the unoccupied shifted energy levels $\varepsilon_{i\sigma}$ may escape the bias window at low bias voltages and bring the device into the Coulomb blockade regime with a negligible tunnelling current.

It is worth mentioning that we implement two additional features in our model: self-consistent calculation of the effective local temperature and classical averaging of spectral fluctuations with a quasi-Boltzmann distribution (see subsec-

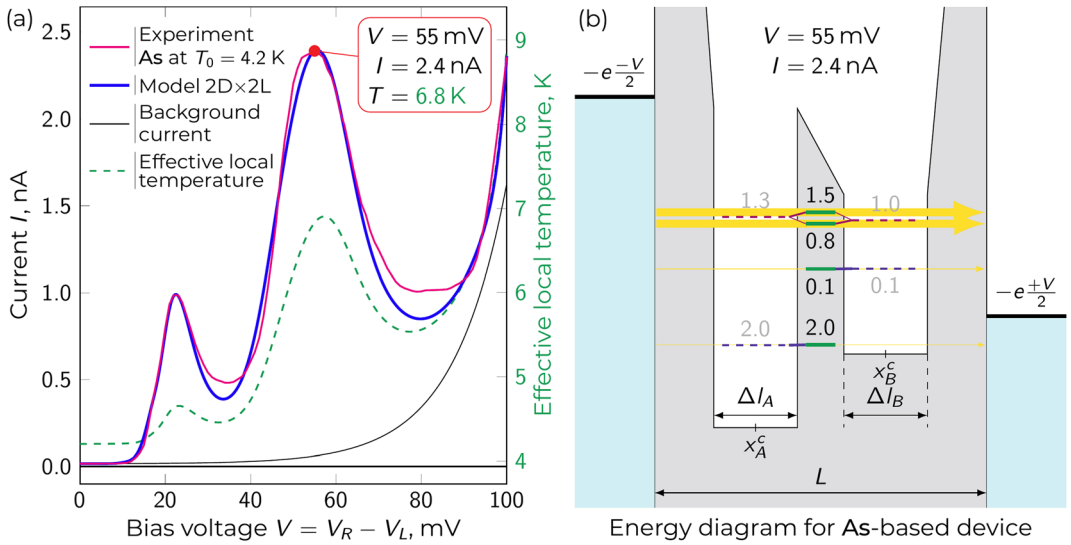

Fig. 4 (a) I–V characteristics of the device based on As obtained from measurements (pink curve) at $V_G^{As} = 2.35$ V and from simulations using the 2D × 2L model (blue curve). Dashed green curve depicts effective local temperature of the nanobridge calculated self-consistently. Background current is plotted in black with $I_{00} = 16.7$ μA, $I_0 = 0.54$ μA, $V_0 = 12.5$ mV. (b) Energy diagram of the 2D × 2L model in the resonant configuration resulting in the current peak (red dot on the I–V curve). Note that the two upper energy levels of dopants align with each other and thus create a more efficient conduction channel. Resonant tunnelling current is indicated with thick yellow arrows. Dimensionless values denote electronic filling factors of the corresponding single-particle and hybridised quantum states. See entry 'As' in Table 1 for the best-fit parameters used. Animated version of this figure is available in the SI.

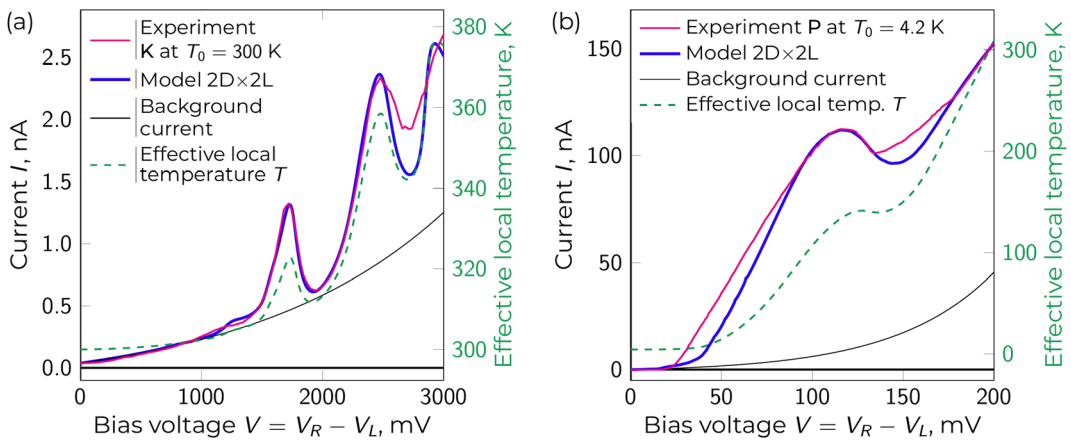

Fig. 5 Pink curves depict I–V characteristics of the measured devices based on K (a) at $V_G^K = -3.9$ V and on P (b) at $V_G^P = 0.0$ V. Best-fit I–V curves of the corresponding 2D × 2L models are plotted in blue. The energy diagrams used are similar to the one shown in Fig. 4b. The corresponding fitting parameters are listed in Table 1. The parameters of the background current curves are: (a) $I_{00} = 38.6$ μA, $I_0 = 220$ μA, $V_0 = 1600$ mV and (b) $I_{00} = 0$ mA, $I_0 = 1.15$ mA, $V_0 = 54$ mV.

Table 1 Best-fit parameters of the 2D × 2L model for devices based on As, K and P (see subsection Model parameterisation of the SI for details)

Dopant	T_0, K	κ, mK pW^{-1}	L, nm	x_A^c, nm	Δl_A, nm	$\Delta\varepsilon_A$, meV	x_B^c, nm	Δl_B, nm	$\Delta\varepsilon_B$, meV
As	4.2	20	20	6.1	5.03	32.1	13.9	5.03	12.2
K	300	10	24	10.5	2.95	208	13.6	2.95	97.5
P	4.2	10	20	7.4	3.00	28.8	12.6	3.00	8.4

tion Effective local temperature and classical fluctuations of the SI for details). The effective local temperature of the nanobridge may be higher than the average temperature of the bulk substrate due to the high power (order of 50 pW or higher) dissipated in the nanosized device that was studied in ref. 37. Therefore, the local nanobridge temperature is expected to

depend on the dissipated power that can be expressed as IV. For simplicity, we assume a linear dependence (5) and introduce a new outer loop for the self-consistent solution of (5). The calculated effective local temperature is plotted as dashed green curves in Fig. 4 and 5, with the scale shown on the right y-axes. Interestingly, our model suggests that the temperature of the P-based device (Fig. 5b) may reach 300 K while its substrate is at the temperature of liquid helium. This seems reasonable since the P-based device dissipates up to 30 nW of power in the nanoscale bridge. The self-heating of the As-based and K-based devices remains relatively mild as long as the dissipated power is smaller than in the P-based device.

The second extra feature of our model is the Boltzmann-like averaging of classical fluctuations experienced by discrete energy levels $\varepsilon_{i\sigma}$. Physically, the fluctuations of $\varepsilon_{i\sigma}$ may occur due to random background charge variations and interaction between the localised electrons and the substrate phonons (hence the potential profile of the dopant wells fluctuates). Since we do not overcomplicate our model with comprehensive quantum description of these two phenomena, it is reasonable to account for them on a semi-classical post-processing stage. Specifically, we calculate tunnelling currents I for an ensemble of similar model entities differing only by variations of $\varepsilon_{i\sigma} \rightarrow \varepsilon_{i\sigma} + \delta\varepsilon_{i\sigma}$. Then we average these fluctuating values of I with Boltzmann-like exponential weights (see subsection Effective local temperature and classical fluctuations of the SI). Importantly, the temperature is still calculated self-consistently for each model entity, so the averaging distribution is a non-Boltzmann one. As a result, the implemented averaging of classical fluctuations broadens the current peaks on the I–V characteristics (giving up to several times larger peak width) and thus significantly improves the fitting accuracy. Without this semi-classical treatment of background charge fluctuations and electron–phonon interaction, it would be impossible for our model to show good agreement with the measured I–V curves.

Finally, we admit that the fitting accuracy could be better away from the current peak apexes. It seems that our model tends to underestimate the tunnelling current in the nonresonant regime. This can presumably be attributed to the neglection of inelastic tunnelling processes. In a non-resonant configuration, the total tunnelling current may increase if one includes additional conductance channels due to phonon- or photon-assisted inelastic tunnelling. Interaction with substrate phonons or infrared/microwave photons may help the localised electrons tunnel between the localisation sites $\varepsilon_i \neq \varepsilon_j$ even with $|\varepsilon_i - \varepsilon_j| \gg T_{ij}$ and thus enhance the tunnelling conductance under nonresonant conditions.

Conclusions

The main result of this paper is the negative differential resistance that was observed in the measured current–voltage characteristics of K-doped nanobridges at room temperature. To the best of our knowledge, this is the first observation of NDR in single-atom devices at room temperature. The observed current peaks can be explained by the resonant electron tunnelling through the dopants with discrete energy levels. Our numerical calculations based on the model of two sequential two-level dopants tunnel-coupled to the source and drain electrodes agree with the experimental data collected for three types of dopants used in the experiments: arsenic, potassium and phosphorus. The quality of I–V curve fitting has been significantly improved by the two additional features implemented in our model: self-consistent evaluation of the local nanobridge temperature and Boltzmann-like averaging of semi-classical spectral fluctuations. The agreement between the experiment and the simulations can be enhanced further if one accounts for inelastic tunnelling processes.

Silicon dioxide doped with potassium atoms is known to be a dielectric material with a permanent built-in electric charge, also known as electret.[38] It is likely that potassium atoms are trapped on the surface of the nanobridge, which is oxidised under ambient conditions,[39] thus forming an electret material. The electret properties of the potassium-doped silicon dioxide signify the strong single-electron properties, which can be used to build single-electron reservoir devices with higher charging energy.

It is also known that K dopants in silicon can group with vacancies[24] in the same manner as N dopants group with vacancies in diamond.[40] We believe that a number of applications can be envisaged for K–V centres similar to those found for N–V centres in diamond.[41]

Methods

Sample fabrication and measurements

For chip fabrication, we applied the process that is fully compatible with CMOS technology and almost identical to the one utilised in our previous works.[22,23,42,43] The commercially available SoiTec Unibond® SOI wafers had a 55 nm (As, P doped) and a 110 nm (K doped) thick top Si layer with a resistivity of 10 Ω cm. It was isolated from the 725 μm thick Si handle wafer with the same resistivity by a 145 nm (As, P doped) and 200 nm (K doped) thick buried oxide layer of SiO_2. The details of the implantation of As and P are described in ref. 22, 23, 42 and 43, respectively.

Implantation of potassium in Si was carried out in the HVEE 500 heavy ion accelerator based on the MSU accelerator complex.[44] For this, a stable current ion source was built, with a cathode made from alkali metal aluminosilicates.[45] Potassium aluminosilicate was obtained by heating a paste of finely dispersed chemical compounds (K_2CO_3, Al_2O_3, $2SiO_2$) dissolved in methanol on tungsten filaments in a rarefied atmosphere.

The top Si layer was doped with K ions at a low surface dose ($n \sim 10^{12}$–10^{13} cm^{-2}) and low acceleration voltage (300 V). At such voltages, K ions are implanted in the near-surface layer penetrating into Si at a depth of about 5 nm. For the given dopant areal density, one can estimate the average separation

between the dopants of 6 ± 3 nm. We can thus conclude that electronic transport in our device occurs *via* individual dopant centres. Also, in such implantation regimes, the Si crystal lattice remains almost undamaged by the ion beam,[46,47] hence, high temperature thermal annealing is not needed for this type of samples.

The fabrication process is based on the conventional top-down approach, in which a narrow nanobridge containing individual dopant atoms is shaped in the initially doped top Si layer of the SOI wafer. First, the desired pattern is formed in resist by electron-beam lithography (Zeiss-Supra40 scanning electron microscope equipped with the Raith ELPHY Quantum pattern generator) and then transferred to the Si layer by reactive ion etching in fluorine plasma.

When forming metallic electrodes, special care was taken to minimise the gaps between them all. By using well-controlled electron-beam lithography and the so-called cold development of the resist,[48] we managed to decrease the gap between the source and drain electrodes to below 20 nm, which is essential for K dopants with deep energy levels. The gate electrodes are located at a distance of 5–10 nm from the transistor channel, allowing the gate voltage to be substantially reduced.

The advantage of the developed fabrication method is that, with the open transistor channel, it allows further trimming of the device by successive etching cycles and additional implantation of various dopants.[43]

Theoretical model

To describe electron transport through localised states of dopant atoms, we employ a model of two two-level dopants connected in series. The second-quantised Hamiltonian of Anderson[49] type reads as follows:

$$\begin{aligned}\hat{H} = &\sum_{\zeta k\sigma} \varepsilon_k^{\zeta} \hat{c}_{k\sigma}^{\zeta\dagger} \hat{c}_{k\sigma}^{\zeta} + \sum_{i=1}^{N} \sum_{\sigma=\uparrow,\downarrow} \varepsilon_{i\sigma} \hat{a}_{i\sigma}^{\dagger} \hat{a}_{i\sigma} \\ &+ \sum_{i\zeta k\sigma} (T_{ik\sigma}^{\zeta} \hat{c}_{k\sigma}^{\zeta\dagger} \hat{a}_{i\sigma} + T_{ik\sigma}^{\zeta*} \hat{a}_{i\sigma}^{\dagger} \hat{c}_{k\sigma}^{\zeta}) + \sum_{i\neq j}^{N} T_{ij\sigma} \hat{a}_{i\sigma}^{\dagger} \hat{a}_{j\sigma} \\ &+ \sum_{i} \tilde{U}_{ii} (\hat{n}_{i\uparrow} - \hat{1} n_{i\uparrow}^{0})(\hat{n}_{i\downarrow} - \hat{1} n_{i\downarrow}^{0}) \\ &+ \sum_{i<j} \tilde{U}_{ij} (\hat{n}_i - \hat{1} n_i^{0})(\hat{n}_j - \hat{1} n_j^{0}), \end{aligned} \tag{2}$$

where fermionic operator $\hat{c}_{k\sigma}^{\zeta\dagger}$ creates delocalised electron with quasi-wave vector k, spin $\sigma \in \{\uparrow,\downarrow\}$ and energy $\varepsilon_k^{\zeta} = \frac{\hbar^2 k^2}{2m} - \mu_{\zeta} - eV_{\zeta}$ in the conduction band of electrode $\zeta \in \{L, R\}$ (Fermi energy $\mu_{\zeta} \sim 5$ eV, effective mass $m \sim m_e$). Electrostatic potentials (such as eV_{ζ}) refer to the Fermi level of the grounded substrate, thus the actual Fermi levels of the source and drain electrodes are equal to $-eV_L$ and $-eV_R$, respectively. The fermionic operator $\hat{a}_{i\sigma}^{\dagger}$ creates an electron that occupies the i-th localisation site with spin σ and energy $\varepsilon_{i\sigma}$. Since the measured I–V curves exhibit two current peaks, we include two discrete energy levels in the spectrum of each dopant. Thus, the index i denotes $N = 4$ levels with $i = 1, 2$ in the left dopant and $i = 3, 4$ in the right dopant. The spectra of both dopants can be shifted linearly with a common gate potential.

Elastic quantum-mechanical tunnelling events are introduced with the help of internal tunnel amplitudes $T_{ij\sigma}$ (processes $i\sigma \leftrightarrow j\sigma$) and external tunnel amplitudes $T_{ik\sigma}^{\zeta}$ (processes $\zeta k\sigma \leftrightarrow i\sigma$) that are assumed to be proportional to the quantum-mechanical transparencies of the corresponding potential barriers derived from geometric dimensions of the system as discussed in subsection tunnelling rates of the SI. Inelastic tunnelling assisted by phonons or photons is neglected. Coulomb repulsion between localised electrons is represented by terms with Coulomb energies $\tilde{U}_{ij}$ and filling number operators $\hat{n}_{i\sigma} = \hat{a}_{i\sigma}^{\dagger}\hat{a}_{i\sigma}$ and $\hat{n}_i = \hat{n}_{i\uparrow} + \hat{n}_{i\downarrow}$. The Coulomb energies are defined as two-particle electron repulsion integrals between the hydrogen-like wavefunctions chosen as effective molecular orbitals of the localised electrons. The parameters of these Gaussian-type orbitals also depend on geometric dimensions as suggested in subsection Coulomb energies of the SI. Reference filling factors $n_{i\sigma}^0$ correspond to the electrically neutral electronic configuration of impurity atoms and renormalise their discrete energy spectra $\varepsilon_{i\sigma}$ (see subsection Coulomb energies of the SI as well). Furthermore, discrete energy levels $\varepsilon_{i\sigma}$ are subject to classical fluctuations originating from background charge noise and the discarded electron–phonon interaction. We account for these fluctuations and self-heating of the devices as discussed in subsection Effective local temperature and classical fluctuations of the SI.

The scalable FORTRAN implementation[50] of the non-equilibrium diagram technique equations is used to calculate the stationary electric current for the given bias and gate voltages. The general self-consistent calculation iteratively refines electronic filling factors until each of the stationary retarded and lesser Green's functions (their Fourier images) converges to a value corresponding to the stable solution of the self-consistent simultaneous Dyson and Keldysh equations:

$$\begin{aligned} G_{ij\sigma}^{R}(\omega) &= \left[\hat{G}_{\bullet\bullet\sigma}^{0R}(\omega)^{-1} - \hat{\Sigma}_{\bullet\bullet\sigma}^{RT}(\omega) - \hat{\Sigma}_{\bullet\bullet\sigma}^{RC}(\omega)\right]_{ij}^{-1}, \\ G_{ij\sigma}^{<}(\omega) &= \sum_{i'j'} G_{ii'\sigma}^{R}(\omega) \hat{\Sigma}_{i'j'\sigma}^{<T}(\omega) G_{j'j\sigma}^{A}(\omega), \end{aligned} \tag{3}$$

where $G_{ij\sigma}^{0R}(\omega) = \delta_{ij}/(\hbar\omega - \varepsilon_{i\sigma} + i0)$, the stationary advanced Green's function $G_{ij\sigma}^{A}(\omega) = [G_{ji\sigma}^{R}(\omega)]^*$ and tunnel and Coulomb interactions reside in the self-energies $\Sigma_{ij\sigma}^{RT}(\omega)$, $\Sigma_{ij\sigma}^{<T}(\omega)$ and $\Sigma_{ij\sigma}^{RC}(\omega)$, respectively (see ref. 50 for details). Once eqn (3) are solved numerically, one evaluates the expression for the electric current through the device,

$$I = \frac{e}{\hbar} \int \frac{\mathrm{d}(\hbar\omega)}{2\pi} \sum_{\sigma} 4Tr(\hat{G}_{\bullet\bullet,\sigma}^{R}(\omega)\hat{\Gamma}_{\bullet\bullet,\sigma}^{L}\hat{G}_{\bullet\bullet,\sigma}^{A}(\omega)\hat{\Gamma}_{\bullet\bullet,\sigma}^{R})[f_L^0(\hbar\omega) - f_R^0(\hbar\omega)], \tag{4}$$

which is obtained in the standard wideband approximation with the tunnelling rates $\Gamma_{ij\sigma}^{\zeta} \simeq \pi\nu_{\zeta}^{0}(-eV_{\zeta})\left|T_{i|k_F|\sigma}^{\zeta} T_{j|k_F|\sigma}^{\zeta*}\right|$, transversal density $\nu_{\zeta}^{0}(\hbar\omega)[1/eV]$ of delocalised states and Fermi distri-

bution functions $f_\zeta^0(\hbar\omega) = \left[1 + \exp\left(\frac{\hbar\omega + eV_\zeta}{k_B T_\zeta}\right)\right]^{-1}$. The formalism of NDT allows for different temperatures $k_B T_\zeta$ of the electrodes. We set them equal $k_B T_L = k_B T_R = k_B T$, although the effective temperature $k_B T$ is calculated self-consistently and accounts for self-heating of the structure due to the high density of the dissipated power. The self-heating of similar nanostructures has already been observed in previous experiments.[37] Consequently, it is reasonable to deduce the effective local temperature T in a self-consistent way rather than to assume a constant substrate temperature T_0 throughout the sample. Specifically, we suggest a simple linear dependence of the effective local temperature on the dissipated power:

$$k_B T \to k_B T(I, V) = k_B T_0 + \kappa IV, \quad (5)$$

with the temperature-to-power coefficient $\kappa \simeq 10$ mK pW^{-1} taken as the lowest bound from the I–V curve fitting (the upper bound remains uncertain). Remarkably, this value is of the same order as one can estimate from ref. 37, Fig. 5. As a result, self-consistent calculation of the effective local temperature makes the broadening of current peaks on I–V curve non-uniform, which further increases the fitting accuracy. Subsection Effective local temperature and classical fluctuations of the SI clarifies the way self-heating affects the averaging process of classical fluctuations for $\varepsilon_{i\sigma}$.

Conflicts of interest

There are no conflicts to declare.

Data availability

Supplementary information: estimation of the characteristic energies of K dopants in Si. Details of theoretical methods. Animated evolution of the energy diagram for the As-based device. See DOI: **https://doi.org/10.1039/d5nr01075f**. Further data that support the findings of this study are available from the corresponding author upon reasonable request.

Acknowledgements

The authors thank Sarkis A. Dagesyan and Ivan V. Bozhev for assistance in sample fabrication and V. Kashcheyevs for useful discussions. The equipment of the "Educational and Methodical Centre of Lithography and Microscopy", M.V. Lomonosov Moscow State University was used. I. K. and V. M. acknowledge support from the Foundation for the Advancement of Theoretical Physics and Mathematics "BASIS". The work was conducted under the state assignment of Lomonosov Moscow State University.

References

1 A. Butterfield and J. Szymanski, *A Dictionary of Electronics and Electrical Engineering*, Oxford University Press, 5 edn, 2018.
2 S. M. Sze, *High-Speed Semiconductor Devices*, Wiley, 2018.
3 S. M. Sze and K. K. Ng, *Physics of Semiconductor Devices*, John Wiley & Sons, 2006.
4 A. I. Ekimov and A. A. Onushchenko, Quantum Size Effect in the Optical Spectra of Semiconductor Micro-Crystals, *Sov. Phys. Semicond.*, 1982, **16**, 775–778.
5 M. Kiguchi, *Single-Molecule Electronics, An Introduction to Synthesis, Measurement and Theory*, Springer, Singapore, 2016.
6 E. Prati and T. Shinada, *Single Atom Nanoelectronics*, Jenny Stanford Publishing, 2013.
7 J. Chen, M. A. Reed, A. M. Rawlett and J. M. Tour, Large On-Off Ratios and Negative Differential Resistance in a Molecular Electronic Device, *Science*, 1999, **286**, 1550–1552.
8 J. Chen, W. Wang, M. A. Reed, A. M. Rawlett, D. W. Price and J. M. Tour, Room-Temperature Negative Differential Resistance in Nanoscale Molecular Junctions, *Appl. Phys. Lett.*, 2000, **77**, 1224–1226.
9 C. Zeng, H. Wang, B. Wang, J. Yang and J. G. Hou, Negative Differential-Resistance Device Involving Two C60 Molecules, *Appl. Phys. Lett.*, 2000, **77**, 3595–3597.
10 S. I. Khondaker, Z. Yao, L. Cheng, J. C. Henderson, Y. Yao and J. M. Tour, Electron Transport through Single Phenylene-Ethynylene Molecular Junctions at Low Temperature, *Appl. Phys. Lett.*, 2004, **85**, 645–647.
11 N. P. Guisinger, M. E. Greene, R. Basu, A. S. Baluch and M. C. Hersam, Room Temperature Negative Differential Resistance through Individual Organic Molecules on Silicon Surfaces, *Nano Lett.*, 2004, **4**, 55–59.
12 M. Grobis, A. Wachowiak, R. Yamachika and M. F. Crommie, Tuning Negative Differential Resistance in a Molecular Film, *Appl. Phys. Lett.*, 2005, **86**, 204102–204104.
13 Z. J. Donhauser, B. A. Mantooth, K. F. Kelly, L. A. Bumm, J. D. Monnell, J. J. Stapleton, D. W. Price, A. M. Rawlett, D. L. Allara, J. M. Tour and P. S. Weiss, Conductance Switching in Single Molecules through Conformational Changes, *Science*, 2001, **292**, 2303–2307.
14 Z. Yan, X. Li, Y. Li, C. Jia, N. Xin, P. Li, L. Meng, M. Zhang, L. Chen, J. Yang, R. Wang and X. Guo, Single-molecule field effect and conductance switching driven by electric field and proton transfer, *Sci. Adv.*, 2022, **8**, eabm3541–eabm3547.
15 Z. Chen, I. M. Grace, S. L. Woltering, L. Chen, A. Gee, J. Baugh, G. A. D. Briggs, L. Bogani, J. A. Mol, C. J. Lambert, H. L. Anderson and J. O. Thomas, Quantum interference enhances the performance of single-molecule transistors, *Nat. Nanotechnol.*, 2024, **19**, 986–992.
16 N. Simonian, J. Li and K. Likharev, Negative Differential Resistance at Sequential Single-Electron Tunnelling through Atoms and Molecules, *Nanotechnology*, 2007, **18**, 424006–424016.

17 H. W. Liu, T. Fujisawa, T. Hayashi and Y. Hirayama, Pauli Spin Blockade in Cotunneling Transport through a Double Quantum Dot, *Phys. Rev. B:Condens. Matter Mater. Phys.*, 2005, **72**, 161305–161308.
18 P. I. Arseev, N. S. Maslova and V. N. Mantsevich, The Effect of Coulomb Correlations on the Nonequilibrium Charge Redistribution Tuned by the Tunneling Current, *J. Exp. Theor. Phys.*, 2012, **115**, 141–153.
19 P. I. Arseyev, N. S. Maslova and V. N. Mantsevich, Correlation Induced Switching of the Local Spatial Charge Distribution in a Two-Level System, *JETP Lett.*, 2011, **94**, 390–396.
20 V. Mantsevich, N. Maslova and P. Arseyev, Tunneling Transport through Multi-Electrons States in Coupled Quantum Dots with Coulomb Correlations, *Solid State Commun.*, 2014, **199**, 33–38.
21 J. Park, A. N. Pasupathy, J. I. Goldsmith, C. Chang, Y. Yaish, J. R. Petta, M. Rinkoski, J. P. Sethna, H. D. Abruña, P. L. McEuen and D. C. Ralph, Coulomb Blockade and the Kondo Effect in Single-Atom Transistors, *Nature*, 2002, **417**, 722–725.
22 V. V. Shorokhov, D. E. Presnov, S. V. Amitonov, Y. A. Pashkin and V. A. Krupenin, Single-Electron Tunneling through an Individual Arsenic Dopant in Silicon, *Nanoscale*, 2017, **9**, 613–620.
23 S. A. Dagesyan, V. V. Shorokhov, D. E. Presnov, E. S. Soldatov, A. S. Trifonov and V. A. Krupenin, Sequential Reduction of the Silicon Single-Electron Transistor Structure to Atomic Scale, *Nanotechnology*, 2017, **28**, 225304–225310.
24 E. I. Zorin, P. V. Pavlov, D. I. Tetelbaum and A. F. Khokhlov, Donor Properties and Diffusion of K in Si, *Sov. Phys. Semicond.*, 1972, **6**, 21.
25 E. I. Zorin, P. V. Pavlov, D. I. Tetelbaum and A. F. Khokhlov, Difference Between the Properties of Na and K Doped Si, *Sov. Phys. Semicond.*, 1972, **6**, 334.
26 J. A. Mol, J. Verduijn, R. D. Levine, F. Remacle and S. Rogge, Integrated Logic Circuits Using Single-Atom Transistors, *Proc. Natl. Acad. Sci. U. S. A.*, 2011, **108**, 13969–13972.
27 J. J. Pla, K. Y. Tan, J. P. Dehollain, W. H. Lim, J. J. Morton, D. N. Jamieson, A. S. Dzurak and A. Morello, A Single-Atom Electron Spin Qubit in Silicon, *Nature*, 2012, **489**, 541–545.
28 M. Fuechsle, J. A. Miwa, S. Mahapatra, H. Ryu, S. Lee, O. Warschkow, L. C. Hollenberg, G. Klimeck and M. Y. Simmons, A Single-Atom Transistor, *Nat. Nanotechnol.*, 2012, **7**, 242–246.
29 G. Yamahata, K. Nishiguchi and A. Fujiwara, Gigahertz Single-Trap Electron Pumps in Silicon, *Nat. Commun.*, 2014, **5**, 1–7.
30 G. C. Tettamanzi, R. Wacquez and S. Rogge, Charge Pumping through a Single Donor Atom, *New J. Phys.*, 2014, **16**, 63036–63052.
31 P. C. Spruijtenburg, S. V. Amitonov, F. Mueller, W. G. van der Wiel and F. A. Zwanenburg, Passivation and Characterization of Charge Defects in Ambipolar Silicon Quantum Dots, *Sci. Rep.*, 2016, **6**, 38127–38133.
32 A. Afiff, A. Samanta, A. Udhiarto, H. Sudibyo, M. Hori, Y. Ono, M. Tabe and D. Moraru, Coulomb-Blockade Transport in Selectively-Doped Si Nano-Transistors, *Appl. Phys. Express*, 2019, **12**, 085004–085008.
33 Y. Meir and N. S. Wingreen, Landauer formula for the current through an interacting electron region, *Phys. Rev. Lett.*, 1992, **68**, 2512–2515.
34 N. S. Maslova, P. I. Arseyev and V. N. Mantsevich, Correlated impurity complex in the asymmetric tunneling contact: an ideal system to observe negative tunneling conductivity, *Sci. Rep.*, 2019, **9**, 15974–15986.
35 L. V. Keldysh, Diagram technique for nonequilibrium processes, *J. Exp. Theor. Phys.*, 1965, **20**, 1018–1026.
36 P. Arseev, On the nonequilibrium diagram technique: derivation, some features, and applications, *Usp. Fiz. Nauk*, 2015, **58**, 1159–1205.
37 V. A. Krupenin, S. V. Lotkhov, H. Scherer, T. Weimann, A. B. Zorin, F.-J. Ahlers, J. Niemeyer and H. Wolf, Charging and heating effects in a system of coupled single-electron tunneling devices, *Phys. Rev. B:Condens. Matter Mater. Phys.*, 1999, **59**, 10778–10784.
38 R. S. Bonilla and P. R. Wilshaw, Potassium Ions in SiO_2: Electrets for Silicon Surface Passivation, *J. Phys. D: Appl. Phys.*, 2017, **51**, 025101–025121.
39 Z. Durrani, M. Jones, F. Abualnaja, C. Wang, M. Kaestner, S. Lenk, C. Lenk, I. W. Rangelow and A. Andreev, Room-temperature single dopant atom quantum dot transistors in silicon, formed by field-emission scanning probe lithography, *J. Appl. Phys.*, 2018, **124**, 144502–144512.
40 M. W. Doherty, N. B. Manson, P. Delaney, F. Jelezko, J. Wrachtrup and L. C. Hollenberg, The nitrogen-vacancy colour centre in diamond, *Phys. Rep.*, 2013, **528**, 1–45.
41 H. H. Vallabhapurapu, I. Hansen, C. Adambukulam, R. Stöhr, A. Denisenko, C. H. Yang and A. Laucht, High-fidelity control of a nitrogen-vacancy-center spin qubit at room temperature using the sinusoidally modulated, always rotating, and tailored protocol, *Phys. Rev. A*, 2023, **108**, 022606–022612.
42 S. A. Dagesyan, V. V. Shorokhov, D. E. Presnov, E. S. Soldatov, A. S. Trifonov, V. A. Krupenin and O. V. Snigirev, Single-Electron Transistor with an Island Formed by Several Dopant Phosphorus Atoms, *Moscow Univ. Phys. Bull.*, 2017, **72**, 474–479.
43 D. E. Presnov, S. A. Dagesyan, I. V. Bozhev, V. V. Shorokhov, A. S. Trifonov, A. A. Shemukhin, I. V. Sapkov, I. G. Prokhorova, O. V. Snigirev and V. A. Krupenin, Single-Electron Structures Based on Solitary Dopant Atoms of Arsenic, Phosphorus, Gold, and Potassium in Silicon, *Moscow Univ. Phys. Bull.*, 2019, **74**, 165–170.
44 A. A. Shemukhin, Y. V. Balakshin, V. S. Chernysh, A. S. Patrakeev, S. A. Golubkov, N. N. Egorov, A. I. Sidorov, B. A. Malyukov, V. N. Statsenko and V. D. Chumak, Fabrication of ultrafine silicon layers on sapphire, *Tech. Phys. Lett.*, 2012, **38**, 907–909.

45 S. K. Allison and M. Kamegai, Lithium Ion Sources, *Rev. Sci. Instrum.*, 1961, **32**, 1090–1092.
46 A. Shemukhin, Y. Balaskshin, A. Evseev and V. Chernysh, The parameter influence of ion irradiation on the distribution profile of the defect in silicon films, *Nucl. Instrum. Methods Phys. Res., Sect. B*, 2017, **406**, 507–510.
47 Y. V. Balakshin, A. A. Shemukhin, A. V. Nazarov, A. V. Kozhemiako and V. S. Chernysh, In Situ Modification and Analysis of the Composition and Crystal Structure of a Silicon Target by Ion-Beam Methods, *Tech. Phys.*, 2018, **63**, 1861–1867.
48 W. W. Hu, K. Sarveswaran, M. Lieberman and G. H. Bernstein, Sub-10 nm Electron Beam Lithography Using Cold Development of Poly(methylmethacrylate), *J. Vac. Sci. Technol., B:Microelectron. Nanometer Struct.–Process., Meas., Phenom.*, 2004, **22**, 1711–1716.
49 P. W. Anderson, Localized Magnetic States in Metals, *Phys. Rev.*, 1961, **124**, 41–53.
50 I. D. Kopchinskii and V. V. Shorokhov, Nonequilibrium Diagram Technique Applied to the Electronic Transport via Tightly Bound Localized States, *Russ. Microelectron.*, 2023, **52**, S337–S351.